Journal of Engineering Mechanics and Machinery (2026)
Clausius Scientific Press, Canada

DOI: 10.23977/jemm.2026.110108
ISSN 2371-9133 Vol. 11 Num. 1

Process-Route Optimization of a Solid Intermediate Shaft for Constant-Velocity Universal Transmission

Jiajun Tang[1,*]

[1]*School of Mechanical Engineering, University of Shanghai for Science and Technology, Shanghai, China*
[*]*Corresponding author*

Keywords: CV Universal Transmission Intermediate Solid Shaft, Equivalent Stress Field, Static-Strength Field, Modal Analysis, Process-Route Optimization

Abstract: This study optimizes the process route of a constant-velocity (CV) universal transmission intermediate solid shaft under specified static-torque and fatigue constraints. A combined analytical-FEA workflow was established for pure torsion and bending-torsion conditions based on assembly test specifications. The critical zone was identified at the spline-root fillet transition. Radial hardness data after induction hardening were converted into a local static-strength field and compared with an ideal demand field derived from equivalent stress and safety-factor requirements. The original route exhibited a subsurface strength depression overlapping with the high-stress region, resulting in the minimum local safety margin. After increasing the lower bound of effective case depth and smoothing the hardness gradient, negative local margins were eliminated and stress-strength matching improved significantly. Modal analysis identified slender low-stiffness sections and vibration-sensitive locations, providing guidance for support placement and spindle-speed window planning. Bench tests showed failure concentration near spline run-out regions, consistent with predictions, while meeting specified performance targets. The proposed stress field-static-strength field-modal coupling framework enables section-wise process control and provides a practical route for reliability-oriented optimization of similar splined shaft components.

1. Introduction

The intermediate solid shaft in CV universal transmission systems performs multiple functions, including torque transmission, compensation of installation misalignment, and adaptation to suspension motion. In service, it operates under complex loading conditions involving alternating torsion superimposed with additional bending moments. Engineering practice has shown that geometric discontinuities, such as spline roots and shoulder fillets, are susceptible to plastic deformation, crack initiation, and premature fracture, often associated with local stress concentration, nonuniform surface strengthening, and residual-stress effects [1-3].

Under concurrent demands for lightweight design and cost control, conventional design methods based only on nominal stress and global safety factors are insufficient to characterize local safety and strength utilization. Previous studies on shafts, drive shafts, and related rotating transmission

components have reported stress concentration, local failure, and fatigue-sensitive behavior at geometric discontinuities [4,5,9-12]. At the process level, turning parameters have been shown to significantly affect residual stress, surface integrity, and fatigue behavior [6,7]. In parallel, strength-degradation theory and stress-strength interference methods provide a useful framework for identifying dangerous and over-strengthened zones through field-level comparisons [8,17].

However, for CV transmission intermediate shafts operating under strict assembly specifications, limited work has addressed how to construct a static-strength field under specific structural and process conditions and evaluate its matching relationship with the actual stress field. Therefore, this study investigates a passenger-car CV transmission intermediate solid shaft and establishes an integrated analysis framework combining pure torsion and bending-torsion loading, static FEA, and modal analysis under assembly-level constraints. Using radial hardness data after induction hardening, the actual static-strength field is obtained via hardness-strength conversion. An ideal static-strength demand field and a local safety-margin index are introduced to evaluate local strength redundancy and potential weak zones across radial positions and axial sections. Modal analysis is further used to identify stiffness-weak and vibration-sensitive regions, providing quantitative guidance for support configuration and turning-speed planning in conjunction with chatter-suppression and slender-shaft machining studies [14-16].

The goal is to develop an integrated stress field-static-strength field-modal characteristic evaluation framework and propose a local-strength-driven process-route optimization strategy for CV transmission intermediate solid shafts, including control of effective hardened depth, section-wise turning-parameter design at critical zones, and coordinated support/stiffness and speed planning.

2. Evaluation Method and Modeling of Static Strength of Solid Shaft in Constant Velocity Universal Drive

2.1 Research Object and Material Process

The object of this study is a solid intermediate shaft in a constant-velocity (CV) universal transmission system for a front-wheel-drive passenger vehicle.

The assembly consists of two CV joints, a solid intermediate shaft, and a splined connection at the differential end; the intermediate shaft has a solid circular cross-section with a minimum diameter of approximately D_{min}=25.6 mm, and the critical section is located at the fillet transition near the spline root.

In design, the intermediate shaft must satisfy both spline-fit constraints and the articulation and plunge functions of the CV joint [13].

As shown in the Fig.1, the maximum articulation angle is 40 ° at the fixed end and 10 ° at the plunging end.

The plunging joint permits axial displacement of the intermediate shaft, and the maximum operating articulation angle varies with the plunge position.

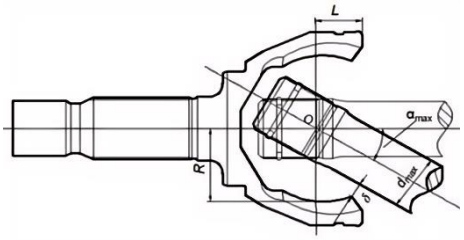

Figure 1. Angular constraint of the fixed joint

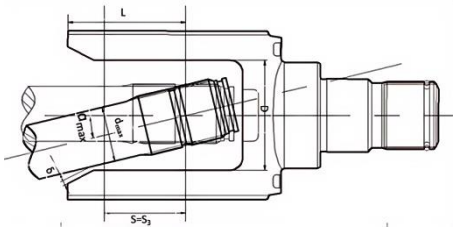

Figure 2. Innermost sliding position of the plunging joint

As shown in Fig. 1, the positional relationship between the fixed-end CV joint and the intermediate shaft is illustrated at the maximum articulation angle ($\alpha = \alpha_{\max}$).

Fig. 2 shows the limit condition when the plunging joint is at its innermost position, where the articulation angle is minimal and increases progressively as the joint moves outward.

The maximum outer diameter of the articulation-constrained section for the fixed/plunging joint segment satisfies the following relation:

$$d_{\max} = 2\cos\alpha_{\max} \cdot (R - L\tan\alpha_{\max}) - 2\delta \tag{1}$$

$d_{\max}$ is the maximum outer diameter of the articulation-constrained section at the fixed/plunging end of the intermediate shaft (mm); R is the spherical radius of the outer race of the fixed/plunging CV joint (mm); L is the distance from the rotation center O of the fixed/plunging CV joint to the outer-race port (mm); $\alpha_{\max}$ is the maximum articulation angle of the fixed/plunging CV joint (°); and δ is the dimensional allowance associated with the boot at the fixed/plunging end (mm).

Considering the above geometric and operating constraints, the maximum outer diameter at both ends is set to 29.5 mm, and the minimum diameter is 25.6 mm.The selected material is UC2 steel (equivalent to a medium-carbon alloy structural steel).

The typical manufacturing route for the intermediate solid shaft includes bar cutting, rough turning of the outer diameter, end-face machining and chamfering, spline pre-machining, induction hardening and tempering, finish turning of the mating sections, and final spline grinding.

The induction-hardening requirements are a surface hardness of 55~62 HRC, a core hardness not exceeding 30 HRC, and an effective hardened depth controlled within 4.5~8 mm based on the 500 HV iso-hardness contour[18-20].

Figure 3. Schematic of the solid shaft part

The assembly static-strength specification defines the following torque limits: at a fixed-end articulation angle of 40°, a plunging-end articulation angle of 10°, and a loading rate of 180°/min, the static torque is MF≥2560 N· m ,when permanent deformation does not exceed 2°,MV≥ 3700 N· m,when macroscopic plastic deformation is permitted, and not less than 4000 N· m at fracture.

The fatigue-strength test is conducted at 7° articulation at both the fixed and plunging ends, with a torque amplitude of ±1245 N· m at 3 Hz, requiring no fewer than 3×10^5 cycles.

These parameters constitute the boundary conditions for the static strength and fatigue life of the intermediate solid shaft.This study focuses on static-strength-field evaluation, taking 3700 N· m as the limit static torque corresponding to the design fracture boundary, while 2560 N· m and 3700

N · m correspond to the yield boundary and the pronounced plastic-deformation boundary, respectively.

2.2 Load Analysis and Stress Field at the Critical Section

During constant-speed rotation, the intermediate solid shaft in a CV universal transmission is primarily subjected to torque T; when the joint operates at an articulation angle, an additional bending moment M_w is imposed on the shaft due to transmission error and geometric characteristics.

In engineering calculations, the additional bending moment can be approximately expressed as:

$$M_w = M_q \tan\delta \tag{2}$$

M_q is the transmitted torque and δ is half of the total articulation angle of the universal joint. Under the extreme condition of 40 ° articulation at the fixed end and 10 ° at the plunging end, the equivalent articulation angle δ can be taken on the order of 10 °, for which $\tan\delta$ is approximately 0.18–0.36, indicating that the additional bending moment is limited relative to the transmitted torque.

Taking the solid circular shaft under torsional loading shown in Fig. 3 as an example, the design method of the static strength field is introduced. The maximum static torsional load during service of the solid circular shaft is taken as 3600 N·m. For the critical section with the minimum diameter D=25.6mm, hollowness is negligible and the section is treated as a solid circular shaft.

Under pure torsion, the shear stress at a radial distance ρ from the shaft center is:

$$\tau(\rho) = \frac{T_\rho}{J_p}, J_p = \frac{\pi D^4}{32} \tag{3}$$

τ is the shear stress and J_p is the polar moment of inertia of the critical section.

The maximum shear stress on the outer surface $\rho = \frac{D}{2}$ is:

$$\tau_{\max} = \frac{16T}{\pi D^3} \tag{4}$$

Given the relatively simple geometry and loading of the circular shaft, mechanics-of-materials analysis indicates that the critical section is located at the outer surface where the torsional section modulus is minimal (i.e., at the minimum diameter), namely at 26.5 mm. The maximum stress at the critical section is:

$$\tau_{\max} = \frac{16\mathrm{T}}{\pi \mathrm{D}^3} = \frac{16\times 3600}{26.5^3\pi} = 985MPa \tag{5}$$

The direction of the maximum static stress gradient extends from the outer surface of the critical section toward the shaft center; the maximum stress at the critical section and the stress at any point along its gradient distribution are calculated as follows:

$$\tau_y = \frac{32Ty}{\pi D^4} = \frac{32\times 4320y}{26.5^4\pi} = 74yMPa \tag{6}$$

T is the torque (N·m), D is the outer diameter of the section (m), and y is the distance to the shaft center.

In this case, the safety factor for static-strength design is set to 1.2; based on the maximum static

stress and its gradient distribution under the structural limit static load, the ideal static-strength-field distribution is determined as shown in Fig. 4, which also presents the structural limit-stress distribution.

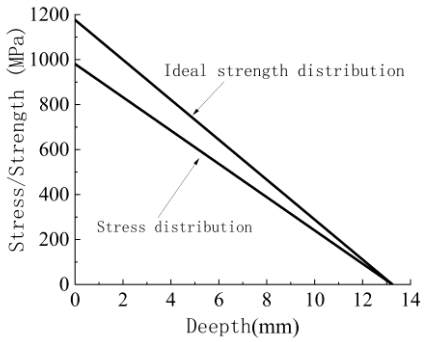

Figure 4. Limit stress distribution and ideal static strength distribution at the critical section

After determining the ideal static strength distribution at the structural critical section, material and heat-treatment matching is carried out with this ideal distribution as the target. The actual static strength distribution achieved through material and heat-treatment matching should be made as consistent as possible with the ideal static strength distribution.

In this case, according to the ideal static strength distribution at the critical section shown in Fig. 4, UC2 steel is selected and medium-frequency surface induction hardening is specified, with required surface hardness of 55~62HRC, hardened depth at the 500 HV level of 4.5~8 mm, and core hardness ≤30HRC.Fig. 5 presents the minimum and maximum hardness–depth curves at the critical section derived from the UC2 end-quench curve in conjunction with the heat-treatment requirements; by applying the hardness-to-strength conversion relationship and the third strength theory, the actual static strength distribution of this structure is obtained, and in this case the conversion between HRC hardness and torsional static strength is:

$$\tau = 0.00816 H_{\mathrm{d}}^{2.88} + 420 \tag{7}$$

τ is the torsional strength at any point in the structure (MPa), and H_d is the hardness at that point (HRC).

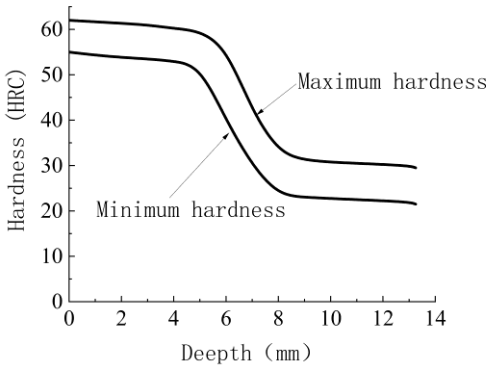

Figure 5. Hardness distribution at the critical section

The actual static strength distribution at the structural critical section, obtained from the HRC-to-torsional-static-strength conversion and the UC2 end-quench curve, is shown in Fig. 6.As shown in Fig. 6, the ideal and actual static strength distributions for this structure are tangent at a subsurface depth of approximately 7.3 mm, which constitutes a critical design point; its strength can be

improved by adjusting the hardened-layer depth and core hardness to increase hardness in the transition region between the hardened layer and the core.

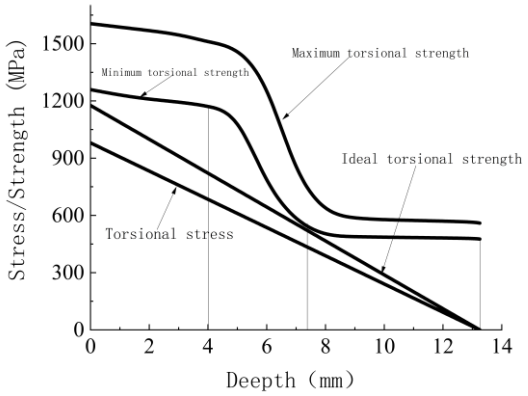

Figure 6. Actual static strength distribution

2.3 Definition of the Ideal Static-Strength Field

To evaluate the utilization of static strength of the intermediate solid shaft under given process conditions, the concept of an “ideal static strength field” is introduced. The ideal static strength field refers to the distribution of minimum required yield strength or shear strength at each radial position, subject to the constraints of limit static torque and the prescribed design safety factor. Taking the critical section as an example, the equivalent stress distribution $\sigma_{eq}(r)$ under the limit static torque of 3700 N·m is used as the design baseline; with the static-strength safety factor specified by enterprise standards or design codes, the ideal static strength field can be expressed as:

$$\sigma_{ideal}(r) = \gamma_s \sigma_{eq}(r) \tag{8}$$

For torsion-dominated loading conditions, an equivalent shear-stress formulation may also be adopted:

$$\tau_{ideal}(r) = \gamma_s \tau(r) \tag{9}$$

The ideal static strength field is determined solely by geometry and loading conditions, independent of specific heat-treatment and machining processes. It defines the minimum strength required at each radial position under the target load level and safety-factor constraint, and serves as the benchmark for subsequent comparison with the actual static strength field.

2.4 Hardness-Strength Conversion and Actual Static-Strength Field

The surface layer of the intermediate solid shaft is treated by induction hardening followed by tempering, resulting in a pronounced radial gradient in microstructure and hardness. Hardness testing on production parts or process specimens provides H(r) at the surface and at different depths, which is then used to construct the actual static strength field. Within an applicable range, material strength and hardness can be approximated as linearly related, for example:

$$\sigma_{ys}(r) \approx aH(r) + b \tag{10}$$

An empirical relationship between shear yield strength and Rockwell hardness may also be adopted:

$$\tau_y(r) \approx kHRC(r) \tag{11}$$

Engineering practice indicates that for materials similar to UC2 steel, the empirical coefficient typically falls within 35~45 MPa/HRC, and a more accurate value can be obtained by least-squares fitting of tensile–hardness data from a set of quenched-and-tempered specimens.

In this study, hardness was measured at radial sampling points within an axial interval near the critical section, yielding maximum and minimum curves that represent the upper and lower hardness bounds under process variability. Using the above conversion relationships, the corresponding maximum and minimum static strength fields were obtained.

2.5 Local Static-Strength Safety Margin

To characterize the degree of local static-strength utilization, a dimensionless static-strength safety margin is introduced:

$$\eta_s(r) = \frac{\sigma_{\min}(r)}{\sigma_{ideal}(r)} \tag{12}$$

When $\eta_s(r) > 1$, the actual static strength at that location exceeds the ideal requirement, indicating strength redundancy; $\eta_s(r) \approx 1$ indicates relatively efficient utilization of static strength; and $\eta_s(r) < 1$ implies a risk of insufficient static strength under the limit static torque, which should be compensated by adjusting the heat-treatment process or geometric dimensions.

By calculating the radial distribution of $\eta_s(r)$ at the critical and adjacent sections and visualizing it together with the equivalent stress field, one can directly identify high-stress/low-margin risk zones and low-stress/high-margin redundant zones, thereby providing a localization basis for subsequent process-chain optimization.

3 Results and Discussion

3.1 Static-Strength Matching Under the Original Process Route

Under the original process scheme, the target hardened-layer depth of the UC2 solid shaft was 4~6 mm. Hardness test results [18-20] indicate that hardness remains essentially at 58~60 HRC within the 0~2 mm surface layer, decreases slightly over 2~4.5 mm, drops markedly near 4.5 mm, and approaches the tempered-core level at a depth of 8 mm, as shown in Fig. 7.

The minimum static-strength field derived from hardness–strength conversion shows relatively high surface static strength, a mid-depth “strength depression,” and a stabilized strength level in the core.

Comparison with the ideal static-strength field shows that at surface point $r \approx \frac{D}{2}$, $\eta_s(r)$ is slightly greater than 1, indicating moderate surface strength redundancy; at a depth of approximately 4.5 mm, $\eta_s(r) < 1$, revealing a weak link with insufficient static strength; and at 8 mm, $\eta_s(r)$ rises again to near 1.

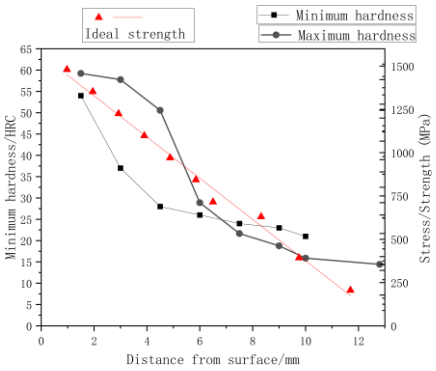

Figure 7. Hardness and hardness-gradient curves at the critical section

This serrated "surface–subsurface–core" static-strength profile implies that under limit static torque, the subsurface region may be the first to yield or initiate microcracks, while the surface and core still retain substantial strength reserve, leading to nonuniform local strength utilization.

Spatially, the fillet at the critical section exhibits the highest equivalent stress under pure torsion, whereas the radial static strength reaches a trough at intermediate depth, resulting in the minimum local safety margin in that region. Although no pronounced static torsional fracture has been observed in current assembly tests, this region may evolve into a static-strength weak zone if the limit load fluctuates or the material performance is lower than expected.

3.2 Strength-Field Evolution after Effective Case-Depth Adjustment

To address the above issue, the induction-hardening parameters were optimized by controlling the effective case depth within 4.5~8 mm and moderately reducing the upper limit of surface hardness, thereby smoothing the hardness distribution within the hardened layer.

The hardness–depth curve under the improved process shows a slight reduction in surface hardness, a pronounced increase in hardness over the 4.5–8 mm range, and a reduced hardness gap before and after tempering.

Converting the updated hardness curve into a static-strength field and comparing it with the ideal static-strength field yields the following features:

At the surface, the actual static strength is slightly higher than the ideal value, with $\eta_s(r) \approx 1.05$.

At a depth of 5 mm, the static strength is substantially higher than the ideal demand, with $\eta_s(r)$ around 1.3, constituting the primary strength-redundant region.

Near 8 mm, the static strength remains slightly above the ideal value ($\eta_s(r) \approx 1.03$), essentially achieving the design objective of "closely tracking the ideal curve."

Compared with the original process, the previously weak subsurface zone where $\eta_s(r) < 1$ is effectively eliminated; across the entire hardened layer, the static-strength safety margin remains positive with reduced fluctuation, the local "short board" is filled, and excessive strength redundancy at the surface and in the core is moderately curtailed.

3.3 Engineering Implications of Redundant and Weak Regions

From a stress-strength interference perspective, the spline-root fillet remains the highest-demand zone. Before optimization, subsurface under-strength made this location the minimum-margin region; after optimization, it shifts to a stable positive margin slightly above unity. In contrast, equal-diameter and noncritical regions maintain higher redundancy under lower equivalent stress,

supporting section-wise process differentiation.

4 Static and Modal Finite Element Analyses

4.1 Static Stress Analysis

The static stress analysis is based on the assembly load and geometric model mentioned above. The stress field of the solid shaft in the constant speed universal joint is solved in the finite element software. The boundary condition is applied by the torque at one end and the constraint at the other end. The load is 3700 Nm torque and the additional bending moment caused by the universal joint swing angle is considered.The resulting equivalent-stress distribution is shown in Fig. 8.

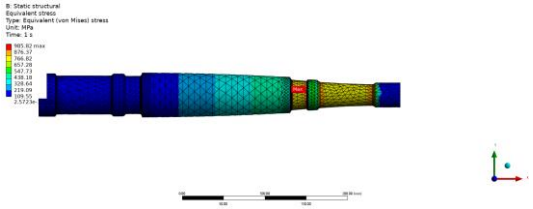

Figure. 8 Static stress distribution

The simulation results indicate that the critical section remains located at the spline-root fillet transition, with a peak value of 985.82 MPa, which is comparable to the preceding calculation.Finite-element results further show that under both pure torsion and combined bending–torsion conditions, the maximum equivalent stress is concentrated near the spline-root fillet transition; the predicted critical location is consistent with the analytical result, and the additional bending moment introduces only a limited increment in equivalent stress without altering the critical-section location or the principal stress direction.Therefore, static-strength evaluation can adopt a torsion-dominant modeling approach supplemented by bending-moment correction.

From the axial distribution perspective, stress exhibits clear geometric sensitivity along the shaft: pronounced concentration occurs at geometric discontinuities such as reduced-diameter segments, fillets, and shoulders, whereas stress in long constant-diameter segments is relatively uniform and decays gradually.The static stress concentration identified in the simulated critical regions suggests that these locations are prone to fatigue-crack initiation under limit loading; accordingly, residual-stress and surface-quality control in these regions should be prioritized during turning and heat-treatment processes.

4.2 Modal Analysis

Modal analysis yielded the first three modes, and the corresponding mode shapes are shown in Figs. 9-11.

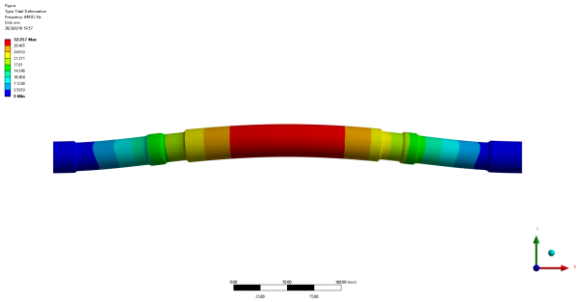

Figure. 9 First mode shape

As shown in Fig. 9, the 1st mode (~649.82 Hz) has the maximum deflection at the slender mid-span segment;

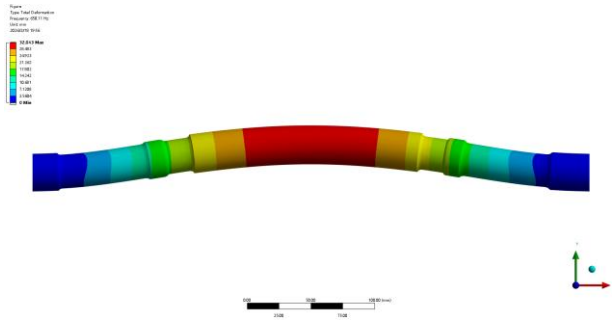

Figure. 10 Second mode shape

As shown in Fig. 10, the 2nd mode (~650.11 Hz) has an antinode near the spline transition and minimum-diameter segment;

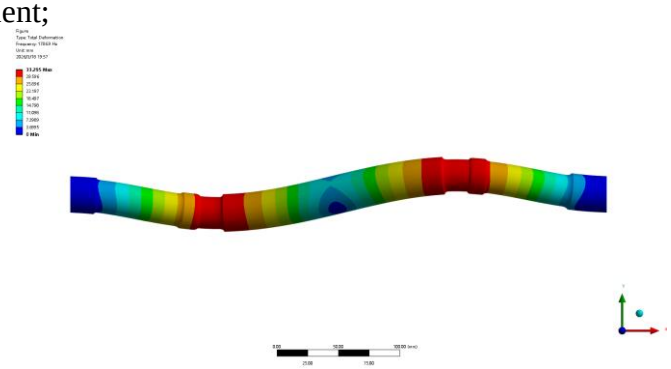

Figure. 11 Third mode shape

As shown in Fig. 11, the 3rd mode (~1786.9 Hz) extends toward the slender segment near the free end. The mid-span slender section is therefore the global stiffness-weak zone.

The combined interpretation of the first three mode shapes shows that the mid-span reduced-diameter segment is the weakest part in terms of global stiffness and the region most susceptible to vibration amplification during machining. Therefore, process design should prioritize increasing support stiffness in this segment and implementing vibration-suppression measures [14-16].

Meanwhile, converting natural frequencies into corresponding spindle-speed ranges enables the definition of resonance-prone speed bands to be avoided in process planning, thereby providing a theoretical basis for spindle-speed selection in actual machining [14-16].

4.3 Implications for Process-Route Optimization

Coupling static and modal results provides both spatial and frequency-domain guidance. Critical sections require tighter turning and heat-treatment control to maintain favorable stress/strength matching. Modal results support center-rest placement near first-mode deflection peaks and spindle-speed planning away from resonance-prone bands.

5 Conclusion

1) A quantitative framework combining ideal-demand and actual static-strength fields was established for CV intermediate solid shafts under assembly-level constraints, enabling visualization of weak and redundant zones.

2) Under the original route, a subsurface strength short board exists in the critical section.

Controlling effective case depth to 4.5-8 mm and smoothing hardness gradients eliminates local negative margin and improves margin distribution.

3) Static and modal FEA confirmed the critical stress location and identified the slender mid-span as the primary vibration-sensitive region, providing quantitative guidance for support placement and spindle-speed planning.

4) A partitioned process-chain strategy is proposed: quality-priority control for critical sections and efficiency-priority control for redundant sections.

Declarations

The authors declare that they have no competing interest.

References

[1] Capello E (2005) Residual stresses in turning: Part I: Influence of process parameters. Journal of Materials Processing Technology 160(2):221-228.https://doi.org/10.1016/j.jmatprotec.2004.06.012

[2] Díaz-Salamanca D, et al (2024) Influence of turning parameters on residual stresses and surface roughness in SAE 1045 steel. The International Journal of Advanced Manufacturing Technology.

[3] Maranhão C, Davim JP (2008) Influence of machining parameters on residual stress and surface integrity in turning. The International Journal of Advanced Manufacturing Technology 36:109–116.

[4] Bayrakceken H, Tasgetiren S, Yavuz I (2007) Two cases of failure in the power transmission system: An universal joint yoke and a drive shaft. Engineering Failure Analysis 14(4):716–724. https://doi.org/10.1016/j.engfailanal.2006.04.001

[5] Göksenli A, Eryürek IB (2009) Failure analysis of an elevator drive shaft. Engineering Failure Analysis 16(4):1011–1019. https://doi.org/10.1016/j.engfailanal.2008.05.014

[6] Vogwell J (1998) Analysis of a vehicle wheel shaft failure. Engineering Failure Analysis 5(4):271–277.https://doi.org/10.1016/S1350-6307(98)00022-3

[7] Qu Y, Meng Q, Zhang D, et al (2022) A modified strength degradation model of 45 steel under cyclic loading. Australian Journal of Mechanical Engineering.

[8] Jiang X, Wang J, Jiang T, et al (2022) An improved nonlinear cumulative damage model based on strength degradation considering loading sequence. International Journal of Damage Mechanics 31(5):799–824.

[9] Wang HJ, Liu XQ, Wang D, et al (2020) Prediction and evaluation of fatigue life under random load. Theoretical and Applied Fracture Mechanics 110:106346.

[10] Wu JB, Wang P, Li JJ (2019) Research on diameter tolerance of transmission shaft based on interval analysis. Journal of Failure Analysis and Prevention 19:726–734.

[11] Zulhilmi AA, Abdullah S, Ghazali MJ, et al (2012) Finite element analysis and fatigue analysis of spur gear under random loading. Advanced Materials Research 457–458:1186–1190.

[12] Shokrieh MM, Hasani H, Lessard L (2004) Shear buckling of a composite drive shaft under torsion. Composite Structures 64(1):63–69.https://doi.org/10.1016/S0263-8223(03)00214-9

[13] Wang JW (2014) Design and Analysis of Constant Velocity Joints and Driveshaft Systems. National Defense Industry Press, Beijing. (in Chinese)

[14] Munoa J, Beudaert X, Dombovari Z, et al (2016) Chatter suppression techniques in metal cutting. CIRP Annals - Manufacturing Technology 65(2).https://doi.org/10.1016/j.cirp.2016.06.004

[15] Cai W, Xiang J, Dong G, et al (2025) Analytical modelling of parallel multidirectional cutting of slender shafts. International Journal of Mechanical Sciences 288:110024.

[16] Sun Y, Zheng M, Zhang X, et al (2023) A state-of-the-art review on chatter stability in machining thin-walled parts. Machines 11(3):359.

[17] Menan F, Adragna PA, François M (2015) The stress-strength interference method applied to fatigue design: The independence of the random variables. Procedia Engineering133:746-757.https://doi.org/10.1016/j.proeng.2015.12.656

[18] National Standard of the PRC (2005) GB/T 5617-2005 Determination of effective depth of hardening after induction or flame hardening of steel. Published 2005-07-21, implemented 2006-01-01.

[19] National Standard of the PRC (2025) GB/T 5617-2025 Determination of case depth of surface-hardened steel parts. Published 2025-08-29, implemented 2026-03-01.

[20] ISO 3754:1976 Steel—Determination of effective depth of hardening after induction or flame hardening. International Organization for Standardization.